Exploring the flow of immiscible fluids in a square vertical mini-channel by direct numerical simulation

B.E. Ghidersa *,   M. Wörner, D.G. Cacuci

Forschungszentrum Karlsruhe, Institut für Reaktorsicherheit, Postfach 3640, 76021 Karlsruhe, Germany

Abstract

The three-dimensional flow structure of a bubble-train flow in a square capillary of 2 mm width is investigated numerically. Using the volume of fluid method for tracking the phase interface direct numerical simulations in a cubic flow unit cell are performed for a void fraction $\varepsilon = 33\%$ and two different values of the Capillary number ($Ca_B = 0.205$ and $Ca_B = 0.043$). Comparison of computed global flow parameters with available experimental data shows good agreement. Though for both Capillary numbers the bubble is fully axisymmetric, quite different flow structures in the bubble and in the liquid slug are observed. This suggests that the flow conditions in miniaturized devices for chemical processing involving two-phase flow in square or rectangular mini- or micro-channels are very sensitive, indicating a certain potential for careful optimization.

Key words: Bubble train flow, Taylor bubble, Square mini-channel, Direct numerical simulation
PACS:

1   Introduction

Within the last decade great progress has been made in the development of advanced technologies for fabrication of miniaturized devices such as micro-heat exchangers and micro-reactors [1–4]. Compared to equivalent devices of conventional size these micro-devices offer some potential advantages [2,5] not

---

* Corresponding author.
   Email address: ghidersa@irs.fzk.de (B.E. Ghidersa).

only for single-phase flows but also for multi-phase flows, which are of certain relevance for a number of basic operations in chemical engineering. The micro-bubble column reactor [2] for example can provide for extraordinary high interfacial area per unit volume [6] and thus allows for high mass transfer rates. Another example is the segmented flow tubular reactor [7] developed within the bubble tube project that utilizes the intense mixing of the two-phase flow for production of high-quality powder.

Miniaturized devices for chemical processing often consist of large number of nominally identical parallel channels. Therefore, a pre-requisite for design, optimization and safe operation of a multi-phase micro-reactor is the understanding of the basic hydromechanical phenomena within a single channel. This is the motivation for an increasing number of analytical [8–10] and experimental studies devoted to the two-phase flow in single narrow tubes [11–13] and in channels with triangular [11,12] or rectangular [15,16] cross-section.

When the hydraulic diameter of the channel is very small measurement techniques that are well established in macro-channels encounter serious difficulties. In micro-channels only non-intrusive measurement techniques can be used and the results are usually limited to visualization of the bubble shape and measurement of integral data such as the flow rates of both phases and the axial pressure drop. This is along the main objectives of many experimental studies, namely to develop engineering correlations for pressure-drop [12] and heat transfer. A second objective of experimental studies is to develop flow regime maps that allow to predict the two-phase flow pattern [11]. In two-phase flow in mini- and micro-channels surface tension effects dominate. Therefore, the walls are usually wetted and a liquid layer separates the gas from the channel walls. For immiscible fluids three main flow regimes are observed: bubbly flow, slug flow and annular flow. These flows are essentially laminar, bubble break-up or coalescence hardly occur and stable bubbles and thin liquid films can be obtained.

Recently, great progress has been made in the development of the micro particle image velocimetry (PIV) method [17] and the stereoscopic micro PIV method [18]. However, these methods are demonstrated for single phase flows only. For two phase flow, there is currently no measurement method available that can provide full information on the three-dimensional local velocity field of both phases in the entire mini- or micro-channel.

In the present study we use the method of direct numerical simulation (DNS) in combination with the volume of fluid method for interface tracking to investigate the slug flow of two immiscible fluids in a straight square mini-channel. In the context of single phase flows DNS usually refers to turbulent flows. Here, the two-phase flow is laminar and the use of the term DNS expresses the fact that in the simulation all scales of both, the velocity field and the

phase interface are fully resolved. The flow consists of a regular train of bubbles which occupy most of the channel cross-section and are often denoted as Taylor bubbles. The individual bubbles are separated by liquid slugs which are, in narrow channels, free of smaller bubbles. This type of flow is also referred as bubble-train (BT) flow [15]. The devices for which our simulation results are of relevance include e.g. the micro bubble column [2,6] and the monolith froth reactor [19].

The physical parameters of the simulations to be presented in this paper correspond to experiments of Thulasidas et al. [15] for air bubbles in silicone oil flowing co-currently in a vertical square channel with 2 mm side length. Results of two simulation runs are presented. These correspond to different values of the Capillary number, which is the relevant non-dimensional group for two-phase flow in small channels. The influence of the Capillary number on the bubble shape and flow inside and outside the bubble is discussed. As it will be shown, our numerical results provide descriptions of the flow at a level of detail that far exceeds the insight one can get from experiments alone.

The organization of this paper is as follows. In section 2 we list the governing equations and shortly describe the numerical method of our in-house DNS computer code TURBIT-VOF used to perform the simulations. Section 3 is devoted to the verification of the results by experimental data and a detailed analysis of the bubble shape and flow structure. In section 4 we present the conclusions.

2 Computational setup

2.1 The unit cell concept

Characteristic to micro-channels is the large ratio between channel length and hydraulic diameter. For the flow of incompressible immiscible fluids one can, therefore, identify a region where entrance effects have diminished and bubbles of identical shape are uniformly distributed along the channel and move with constant velocity. Thus, a "unit cell" consisting of a bubble and the slug in the rear of the bubble can be defined. Such a unit cell fully characterizes the developed bubble-train (BT) flow. Optical measurements are often done by following the unit cell in its movement along the channel by a moving camera. In our numerical approach, we define the computational domain such that it has the same dimensions as the unit cell. This domain is fixed in space while the bubbles move through it (see Figure 1). The presence and influence of the trailing and leading unit cells is simulated by periodic boundary conditions in axial direction together with a constant body force that represents a prescribed

constant axial pressure drop.

2.2   Governing equations

We consider the flow of two incompressible Newtonian fluids separated by a phase interface. We denote the continuous fluid as "liquid" (index l) and the disperse one as "gas" (index g). To describe the time and space evolution of the phase interface we use the volume of fluid method (VOF) [20]. The basic idea of the VOF method is the definition of a scalar quantity f which represents the fraction of the volume V of a mesh cell occupied by the liquid. Thus, for $f = 1$ the mesh cell is entirely filled with liquid while for $f = 0$ it is entirely filled with gas. In a mesh cell that instantaneously contains a part of the interface both phases coexist and it is $0 < f < 1$. Based on f we define the non-dimensional mixture density

$$\rho_m \equiv \frac{f\rho_l^* + (1-f)\rho_g^*}{\rho_l^*} = f + (1-f)\Gamma_\rho \tag{1}$$

and non-dimensional mixture viscosity

$$\mu_m \equiv \frac{f\mu_l^* + (1-f)\mu_g^*}{\mu_l^*} = f + (1-f)\Gamma_\mu, \tag{2}$$

where we use the physical properties of the liquid phase as reference values. Note that throughout the paper the superscript * is used to indicate a dimensional quantity. Using U_{ref}^* as a reference velocity scale, we introduce the non-dimensional center-of-mass velocity

$$\mathbf{v}_m \equiv \frac{1}{U_{\text{ref}}^*} \frac{f\rho_l^*\mathbf{v}_l^* + (1-f)\rho_g^*\mathbf{v}_g^*}{f\rho_l^* + (1-f)\rho_g^*} \tag{3}$$

Here, $\mathbf{v}_l^*$ and $\mathbf{v}_g^*$ represent the mean liquid and gas velocity within the mesh cell, obtained by volume averaging over the region occupied by the respective phase within V.

Based on the above quantities the equations governing the motion of the liquid and gas phase as well as the dynamic boundary condition at the interface can be combined into one single non-dimensional continuity and momentum equation which are valid in the entire computational domain:

$$\nabla \cdot \mathbf{v}_m = 0 \tag{4}$$

4

$$\frac{\partial (\rho_m \mathbf{v}_m)}{\partial t} + \nabla \cdot \rho_m \mathbf{v}_m \mathbf{v}_m = -\nabla P + \frac{1}{Re_{\mathrm{ref}}} \nabla \cdot \mu_m \left(\nabla \mathbf{v}_m + (\nabla \mathbf{v}_m)^{\mathrm{T}} \right)$$
$$- (1-f)\frac{Eo_{\mathrm{ref}}}{We_{\mathrm{ref}}}\hat{\mathbf{e}}_g + Eu_{\mathrm{ref}}\hat{\mathbf{e}}_p + \frac{a_i \kappa \hat{\mathbf{n}}_i}{We_{\mathrm{ref}}} \quad (5)$$

The definitions of the reference Reynolds number (Re_{ref}), reference Eötvös number (Eo_{ref}), reference Weber number (We_{ref}), and reference Euler number (Eu_{ref}) appearing in (5) are:

$$Re_{\mathrm{ref}} \equiv \frac{\rho_l^* L_{\mathrm{ref}}^* U_{\mathrm{ref}}^*}{\mu_l^*} \quad (6)$$

$$Eo_{\mathrm{ref}} \equiv \frac{(\rho_l^* - \rho_g^*)g^* L_{\mathrm{ref}}^{*2}}{\sigma^*} \quad (7)$$

$$We_{\mathrm{ref}} \equiv \frac{\rho_l^* L_{\mathrm{ref}}^* U_{\mathrm{ref}}^{*2}}{\sigma^*} \quad (8)$$

$$Eu_{\mathrm{ref}} \equiv \frac{|\Delta p^*|}{\rho_l^* U_{\mathrm{ref}}^{*2}} \quad (9)$$

where L_{ref}^* is a reference length scale to be specified.

It is important to note that to allow for the use of periodic boundary conditions Eq. (5) involves the non-dimensional "reduced pressure" P. This is the actual pressure p^* minus liquid hydrostatic pressure plus the constant axial pressure drop $|\Delta p^*|/L_{\mathrm{ref}}^*$, normalized by $\rho_l^* U_{\mathrm{ref}}^{*2}$:

$$P \equiv \frac{p^* - \rho_l^* \mathbf{g}^* \cdot \mathbf{x}^* + (|\Delta p^*|/L_{\mathrm{ref}}^*)\hat{\mathbf{e}}_p \cdot \mathbf{x}^*}{\rho_l^* U_{\mathrm{ref}}^{*2}} \quad (10)$$

Here, $\mathbf{g}^* = g^*\hat{\mathbf{e}}_g$ is the gravity vector and $\hat{\mathbf{e}}_p$ is the unit vector pointing in axial downstream direction. Due to this decomposition, the influence of gravity is accounted for by a term that represents the buoyancy force and involves the unit vector in direction of gravity $\hat{\mathbf{e}}_g$. Similarly, the axial pressure drop results in a body force term that involves $\hat{\mathbf{e}}_p$.

The last term in Eq. (5) expresses the contribution of the surface tension force in the momentum balance for the volume V. There, $\kappa = \kappa^* L_{\mathrm{ref}}^*$ is twice the non-dimensional mean curvature of the interface, $\hat{\mathbf{n}}_i$ is the unit normal vector to the interface, pointing into the liquid, and $a_i = a_i^* L_{\mathrm{ref}}^*$ is the non-dimensional interfacial area concentration within the mesh cell volume V.

To account for the phase-interface evolution, in the volume of fluid method the liquid volumetric fraction is advected using the transport equation

$$\frac{\partial f}{\partial t} + \nabla \cdot f\mathbf{v}_m = 0 \quad (11)$$

This equation is, however, not solved by a difference scheme but in a rather geometrical manner which involves two steps. In the first step, the interface

orientation and location inside each mesh cell is reconstructed using the PLIC (Piecewise Linear Interface Calculation) method EPIRA (Exact Plane Interface Reconstruction Algorithm) that locally approximates the interface in a mesh cell by a plane (for details see [22]). In a second step the fluxes of liquid across the faces of the mesh cell are computed. This ensures that mass is conserved almost with machine accuracy, which is a key advantage of the VOF method as compared e.g. to the level-set and front-tracking method.

The derivation of the above set of equations is given in [23]. Here, the equations (4), (5) and (11) are already in simplified form. Namely, it is assumed that within a mesh cell both phases move with the same velocity (the center-of-mass velocity $\mathbf{v}_m$). This assumption corresponds to a locally homogenous model.

2.3 Numerical method

The direct numerical simulations are performed with our in-house computer code TURBIT-VOF [21,22] which has been modified and improved for small channel applications [24]. In particular, similar to [25], special care is taken when the gradient of the (physically discontinuous) pressure at the phase-interface is computed [24]. To approximate the convective and diffusive terms in the momentum equation a second order central difference scheme on a staggered grid is used. For the discretization of the surface tension term we refer to [22]. To integrate the momentum equation (5) while enforcing the continuity condition (4) a projection method is used. The time integration is done using an explicit third order Runge-Kutta scheme. Further details on the numerical method can be found in [21,24].

2.4 Physical parameters

A suitable dimensionless number to characterize two-phase flow in small channels is the Capillary number $Ca_B \equiv \mu_l^* U_B^* / \sigma^*$, which expresses the ratio of the two dominant forces, namely viscous and surface tension forces. As the Capillary number involves the viscosity of the continuous phase the effects of varying Ca_B are experimentally most easily studied by using fluids of different viscosity. Thulasidas et al. [15] for example investigated the bubble train flow in a square channel with 2 mm side length using air as disperse phase and silicone oil of different viscosities as continuous phase.

In this paper we study the effect of the Capillary number numerically and discuss in detail results of two simulations (BT1 and BT2). In correspondence to [15] we take as continuous phase silicone oil with different viscosity in case BT1 and BT2, respectively. We choose, however, the gas density and

dynamic viscosity 10 times higher than in [15]. This is in order to increase the computational efficiency of our explicit time integration scheme, which results in severe time step restrictions in the case of very low density ratios [26]. The increase of the gas density by a factor of 10 is justified by the results of [27]. This numerical study on the buoyancy driven steady rise of a single ellipsoidal bubble in a plane vertical channel revealed that under proper scaling the bubble shape and the velocity field in the bubble and the liquid are invariant with respect to a variation of the gas-liquid density ratio. In order to keep the ratio of the Reynolds number in the gas and liquid flow similar to the experiment, the gas viscosity is increased in the simulations by a factor of 10, too. Thus, the gas-liquid kinematic viscosity ratio is the same in the experiment and in the simulation.

In Table 1 we list the fluid properties of both simulation runs while in Table 2 we give the values of the reference scales and those of the reference dimensionless groups appearing in the momentum equation (5). Note that the reference Euler number is estimated from the pressure drop of the single phase flow with the same liquid flow rate as in [15]. The main difference between cases BT1 and BT2 is thus the viscosity of the liquid and the Euler number, respectively the axial pressure drop. Note that the reference Euler number is an input parameter to the code, so that the liquid flow rate and the bubble velocity will adjust to this pressure drop during the simulation. Thus, the bubble velocity is not known a priori but is a result of the simulation. The same holds for the Capillary number. Our numerical approach thus differs from experiments where usually the gas and liquid flow rates are prescribed and the pressure drop adjusts.

2.5 Grid parameters, boundary and initial conditions

In this work the coordinate system is defined by taking the y direction as the stream-wise (vertical) direction and x and z as the two wall-normal directions. The gravity vector points in negative y direction, so that we consider the co-current upward flow in a square vertical channel ($\hat{\mathbf{e}}_p = -\hat{\mathbf{e}}_g = \hat{\mathbf{e}}_y$). The computational domain is a cube of size $L_{\mathrm{ref}}^* = 2$ mm and the non-dimensional size is $1 \times 1 \times 1$. This box is discretized by $64 \times 64 \times 64$ uniform mesh cells. Thus, in total 262,144 mesh cells are used and the spatial resolution is about 31 μm. To study the effect of the grid size, for case BT1 an additional simulation is performed with a coarser grid consisting of $48 \times 48 \times 48$ uniform mesh cells. At the four side walls of the square channel no-slip boundary conditions are applied while, as already stated, in stream-wise direction the presence and influence of the neighboring unit cells is simulated by periodic boundary conditions.

The simulations are started from a spherical bubble positioned in the center of the computational domain. The initial bubble diameter is $D_B^* = 1.716$ mm. This corresponds to an overall volumetric gas fraction of $\varepsilon = 33\%$. Due to the incompressibility of the fluids this value is constant throughout the simulation. After a transient and several thousand time steps (see N_t in Table 3) the bubble shape eventually becomes steady. The bubble itself moves along the channel with constant velocity $U_B = U_B^*/U_{\mathrm{ref}}^*$ and the cross-section averaged velocity in the liquid slug, $U_{\mathrm{sl}} = U_{\mathrm{sl}}^*/U_{\mathrm{ref}}^*$, is constant, too. The flow rates of gas and liquid are then also constant in time and the non-dimensional superficial velocities are given by $J_g = \varepsilon U_B$ and $J_l = (1 - \varepsilon)U_{\mathrm{sl}}$. The simulations are performed on a single processor of a Fujitsu/Siemens VPP5000 vector parallel computer and last, for the more CPU-time demanding case BT2, about two weeks.

3   Results and discussion

3.1   Verification

In Table 3 several non-dimensional integral results of the simulation runs are listed. These include the steady state values of the bubble Capillary number, Ca_B, and the bubble Reynolds number, $Re_B \equiv \rho_l^* D_B^* U_B^*/\mu_l^*$. Results are also given for the non-dimensional bubble diameter $D_B = D_B^*/L_{\mathrm{ref}}^*$, which is the diameter of the bubble in the cross-section where the liquid film thickness is smallest. Furthermore, values for the bubble velocity scaled by the total superficial velocity $V = U_B^*/(J_g^* + J_l^*)$ and the relative bubble velocity $W = (U_B^* - U_{\mathrm{sl}}^*)/U_B^*$ are given. We see that for case BT1 the difference of the results on grid 48^3 and 64^3 are very small. In the following we discuss only the results obtained on the finer grid.

Comparing our numerical values for V and W with the experimental data reported in [15] we find good agreement for case BT1 and BT2, see [14] for a comparison in graphical form. We note, however, that the computed values of D_B are slightly lower than those measured in [15]. We attribute this difference to the fact that in the experiment the bubble length is several times the channel width and the diameter is measured in the cylindrical part while in our computations with a cubic unit cell the bubbles are much shorter and can not develop in elongated Taylor bubbles.

8

3.2 Bubble shape and liquid film thickness

Figure 2 shows the computed steady bubble shape for case BT1 and BT2. The generally accepted minimum value of the Capillary number for which the bubble shape remains axisymmetric (i.e. the bubble cross-section at any axial position is circular) is $Ca_{axi} = 0.04$ [8,15]. In case BT1 the value of Ca_B is 0.205 and thus is about five times higher than Ca_{axi}. The bubble has indeed everywhere a circular cross-section while it is rather elongated, see Fig. 2 a) and c). The minimum thickness of the liquid film is about 10% of L_{ref}^*. In case BT2, where the liquid is 10 times less viscous as compared to case BT1, the Capillary number has a value of 0.043 and the bubble is still axisymmetric, see Fig. 2 d). As Ca_B is still slightly larger than Ca_{axi}, this result is in agreement with [15]. However, a comparison of Figures 2 a) and c) with 2 b) and d) shows that with decreasing value of Ca_B the bubble diameter D_B becomes larger. Therefore, in case BT2 the minimum thickness of the liquid film is only about 4% of L_{ref}^*, i.e. about 80 μm.

3.3 Flow structure in the bubble

The mixing inside the bubble is of great interest in applications where the bubbles are used as micro-reactors in which the precipitation reagents are to be thoroughly mixed [7] avoiding the heterogeneous reaction conditions in classical large batch reactors. In addition to the computed steady bubble shape Figure 2 shows for both cases the flow structure inside the bubble, visualized for a referential system linked to the bubble. These visualizations are obtained by inserting mass-less particles at different positions inside the bubble and observing their advection by the velocity field. For case BT1 the flow in the bubble forms a single toroidal vortex. Instead, in case BT2 the lower viscosity of the liquid determines the appearance of a second vortex at the rear of the bubble. The origin of this second vortex will be discussed below.

We already noted that the shape of the bubble is axisymmetric in both cases. Fig. 2 c) shows that for the higher value of Ca_B the particle trajectories lie almost within a plane, indicating that the flow inside the bubble in this case is almost axisymmetric, too. In contrast, for the lower value of Ca_B the motion inside the bubble is clearly three-dimensional, see Fig. 2 d).

3.4 Flow structure in the liquid

For applications like heat exchangers and in chemical processing, when the re-action is triggered by a catalyst deposed on the wall (monolith froth reactors),

the structure of the flow inside the liquid is more important. In Fig. 3 the flow in the liquid layer between the bubble and the walls and in the liquid slug is presented for case BT1 and BT2. Again, a referential linked to the bubble is used. The massless particles are inserted in front of the bubble ($y = 1$). At the corner of the channel the particles have a rectilinear trajectory and their velocity is almost constant along the channel. Close to the bubble particles are accelerated as they approach the cross-section where the bubble has its largest diameter, and then decelerate, some of the particles being captured in the vortex behind the bubble for case BT2 (Fig. 3 b). For case BT1 the particles are not trapped in the liquid slug.

Thulasidas et al. [16] used a particle image velocimetry to determine the velocity distribution inside the liquid slug. Video images recorded in a reference frame moving with the bubble indicate the presence of recirculating patterns with a high degree of mixing. Depending on the Capillary number of the flow, counter rotating vortices or a complete bypass flow inside the liquid slug are observed. The liquid flow structures of our computations visualized in Fig. 3 do qualitatively agree with this observation.

In Figure 4 the transverse distribution of the axial velocity component in the liquid is presented for case BT1 and BT2, both in the middle of the slug (Fig. 4 a and b) and in the cross-section with the smallest film thickness (Fig. 4 c and d). In the slug region the liquid is moving in stream-wise direction. The velocity profile is similar to that of laminar single-phase flow except for the center of the channel where the profile is flattened due to the recirculation movement behind the bubble. This effect is more significant in case BT2 (Fig. 4 b) due to the lower viscosity of the liquid. For the cross-section with the smallest film thickness, in the liquid film surrounding the bubble a back flow region has been found for both cases (Fig. 4 c and d). This flow corresponds to a local high positive pressure gradient due to the rapid change in film thickness. For case BT2 a second back flow appears in the corners of the channel (Fig. 4 d).

3.5 Coupling of flow in the bubble and the liquid

The above results demonstrate that the flow inside and outside of the bubble is strongly coupled. Due to the relative motion between the bubble and the liquid a vortex is induced within the bubble. In case BT1 this vortex is almost axisymmetric and fills the entire bubble (Fig. 2 a). In case BT2 it fills the most part of the bubble, while at the rear a second vortex appears (Fig. 2 b). Obviously, this vortex is driven by the strong recirculatory motion in the liquid slug (Fig. 3 b).

10

For case BT2 the vortices are not axisymmetric but show a three-dimensional behavior (Fig. 2 d). This loss of symmetry as compared to case BT1 can be explained by the flow in the liquid. The decrease of the Capillary number from case BT1 to case BT2 by a factor of five is associated with a thickening of the bubble and a thinning of the liquid film. This thinning of the liquid film makes the liquid flow within an axial cross section more non-uniform, see Figures 4 c) and d). The thinner the liquid film the more liquid is, in a cross-section upstream of this position, pushed towards the four channel corners. A comparison of Figures 4 c) and d) clearly shows the larger variation of the axial liquid velocity at the circumferential of the bubble in this cross-section for case BT2. In Fig. 4 d) we find small negative values of the axial velocity where the bubble is close to the wall while there are high positive values of the axial velocity at the diagonals of the channel. We conclude that it is this non-axisymmetry of the flow on the liquid side of the interface that causes an enhanced non-axisymmetry of the flow inside the bubble. However, with this process an increased azimuthal mixing inside the bubble is associated which could be of benefit for certain applications.

4 Conclusions

Direct numerical simulations are performed for the co-current pressure-driven bubble train flow in a square vertical channel with 2 mm width. Two simulation runs resulting in two different values of the Capillary number ($Ca_B = 0.205$ and $Ca_B = 0.043$) are compared. For both cases computed global flow parameters agree well with available experimental data. The results for the bubble shape, flow structure within the bubble, and flow structure in the liquid slug are analyzed in detail. The comparison reveals the important role of the Capillary number as the main physical control parameter for two-phase flow in small channels. The decrease of the Capillary number only by a factor of 5 is associated with the thinning of the liquid film, the appearance of a second vortex in the bubble, the enhancement of non-axisymmetry of the flow inside the bubble, and the appearance of a vortex in the liquid slug.

The results obtained show that the two-phase flow conditions in mini- and micro-channels are very sensitive to a variation of the Capillary number. In the present simulation $Ca_B = \mu_l^* U_B^* / \sigma^*$ is varied by using liquids with different viscosity. In practical applications the liquid viscosity (μ_l^*) and the coefficient of surface tension (σ^*) are given. The Capillary number can then only be varied by changing the flow rates, which results in an increase or decrease of the bubble velocity (U_B^*). Our results thus suggest that there might be a certain potential for careful optimization of miniaturized devices for chemical processing involving two-phase flow in square or rectangular channels.

To the author's knowledge, this study represents the first direct numerical simulations of the flow of immiscible fluids in a small square channel. Though the use of a cubic domain, i.e. a cubic two-phase unit cell, seems to be rather restrictive and only two cases are considered, the results nevertheless indicate the potential benefit of the numerical approach. It is demonstrated that using fluid properties and global parameters such as void fraction and axial pressure drop as input, the DNS method in combination with a volume-of-fluid technique for tracking the phase-interface can be successfully used to gain detailed physical insight in the local characteristics of two-phase flow in mini- and potentially micro-channels, not attainable by today's even most advanced experimental techniques. Currently, further simulations for case BT1 are in progress, where the influence of the axial length of the unit cell as well as the influence of the orientation of gravity (horizontal channel) are investigated.

Acknowledgement

Nomenclature

a_i	interfacial area concentration (-)
Ca	Capillary number (-)
D_B^*	bubble diameter (m)
$\hat{\mathbf{e}}_g$	unit vector in direction of gravity (-)
$\hat{\mathbf{e}}_p$	unit vector in direction of axial pressure drop (-)
Eo	Eötvös number (-)
Eu	Euler number (-)
f	liquid volumetric fraction (-)
g^*	gravitational acceleration (m²/s)
J^*	superficial velocity (m/s)
L_{ref}^*	reference length (m)
N_t	number of time steps computed (-)
p^*	pressure (Pa)
P	reduced pressure (-)
Re	Reynolds number (-)
t	time normalized by $L_{\text{ref}}^*/U_{\text{ref}}^*$ (-)
Δt	time step width (-)
U_B^*	bubble velocity (m/s)

U_{ref}^* reference velocity (m/s)

U_{sl}^* slug velocity (m/s)

$\mathbf{v}$ velocity field (-)

V dimensionless bubble velocity (-)

W relative bubble velocity (-)

We Weber number (-)

x, y, z Cartesian co-ordinates (-)

Greek symbols

ε Overall gas void fraction (-)

Γ_μ Gas-liquid viscosity ratio (-)

Γ_ρ Gas-liquid density ratio (-)

μ^* dynamic viscosity (Pa s)

ρ^* density (kg/m^3)

σ^* coefficient of surface tension (N/m)

Subscripts

B bubble

g gas phase

i interface

l liquid phase

m mixture quantity

ref   reference quantity

sl   slug

Superscripts

*   dimensional quantity

ˆ   unit-vector

References

[1] K. Schubert, J. Brandner, M. Fichtner, G. Linder, U. Schygulla, A. Wenka, Microstructure devices for applications in thermal and chemical engineering, Microscale Thermophysical Engineering 5 (2001) 17–39.

[2] W. Ehrfeld, V. Hessel, H. Löwe, Microreactors: New technology for modern chemistry, Viley-VCH, Weinheim, 2000.

[3] A. Gavriilidis, P. Angeli, E. Cao, K.K. Yeong, Y.S.S. Wan, Technology and Applications of Microengineered Reactors, Trans. IChemE 80 Part A (2002)

3–30.

[4] J.M. Commenge, L. Falk, J.P. Corriou, M. Matlosz, Optimal design for flow uniformity in microchannel reactors, AIChE Journal 48 (2002) 345–358.

[5] K.F. Jensen, Microreaction engineering - is small better?, Chem. Eng. Sci. 56 (2001) 293–303.

[6] V. Haverkamp, G. Emig, V. Hessel, M.A. Liauw, H. Löwe, Characterization of a Gas/Liquid Microreactor, the Micro Bubble Column: determination of Specific Interfacial Area, in M. Matlosz, W. Ehrfeld, J.P. Baselt (Eds.): Microreaction Technology, IMRET-5: Proc. Fifth Int. Conf. on Microreaction Technology, Springer 2002, pp. 203–214.

[7] N. Jongen, M. Donnet, P. Bowen, J. Lemaître, H. Hofmann, R. Schenk, C. Hofmann, M. Aoun-Habbache, S. Guillement-Fritsch, J. Sarria, A. Rousset, M. Viviani, M.T. Buscaglia, V. Buscaglia, P. Nanni, A. Testino, J.R. Herguijuela, Development of a Continuous Segmented Flow Tubular Reactor and the "Scale-out" Concept - In Search of Perfect Powders, Chem. Eng. Technol. 26 (2003) 303–305.

[8] J. Ratulowski, H.-C. Chang, Transport of gas bubbles in capillaries, Phys. Fluids A 1 (1989) 1642–1655.

[9] W.B. Kolb, R.L. Cerro, The motion of long bubbles in tubes of square cross section, Phys. Fluids A 5 (1993) 1549–1557.

[10] Q. Liao, T.S. Zhao, Modeling of Taylor bubble rising in a vertical mini noncircular channel filled with a stagnant liquid, Int. J. Multiphase Flow 29 (2003) 411–434.

[11] K.A. Triplett, S.M. Ghiaasiaan, S.I. Abdel-Khalik, D.L. Sadowski, Gas-liquid two-phase flow in microchannels, Part I: two-phase flow patterns, Int. J. Multiphase Flow 25 (1999) 377–394.

[12] K.A. Triplett, S.M. Ghiaasiaan, S.I. Abdel-Khalik, A. LeMouel, B.N. McCord, Gas-liquid two-phase flow in microchannels, Part II: void fraction and pressure drop, Int. J. Multiphase Flow 25 (1999) 395–410.

[13] A. Serizawa, Z. Feng, Z. Kawar, Two-phase flow in microchannels, Exp. Thermal Fluid Sci. 26 (2002) 703–714.

[14] B.E. Ghidersa, M. Wörner, D.G. Cacuci, Numerical simulation of bubble-train flow in a small channel of square cross-section, in: T. Schulenberg, M. Ozawa, G. Grötzbach, (Eds.) Proc. German-Japanese Workshop on Multiphase Flow, Karlsruhe, Germany, August 25–27, 2002, Forschungszentrum Karlsruhe, FZKA 6759, March 2003, pp. G1-G9.

[15] T.C. Thulasidas, M.A. Abraham, R.L. Cerro, Bubble-train flow in capillaries of circular and square cross section, Chem. Eng. Sci. 50 (1995) 183–199.

[16] T.C. Thulasidas, M.A. Abraham, R.L. Cerro, Flow patterns in liquid slugs during bubble-train flow inside capillaries, Chem. Eng. Sci. 52 (1997) 2947–2962.

[17] C.D. Meinhart, S.T. Wereley, J.G. Santiago, PIV measurements of a microchannel flow, Experiments in Fluids 27 (1999) 414–419.

[18] H. Klank, G. Goranvić, J.P. Kutter, H. Gjelstrup, J. Michelsen, C.H. Westergaard, PIV measurements in a microfluidic 3D-sheathing structure with three-dimensional flow behaviour, J. Micromech. Microeng. 12 (2002) 862–869.

[19] A.A. Klinghoffer, R.L. Cerro, M.A. Abraham, Influence of Flow Properties on the Performance of the Monolith Froth Reactor for Catalytic Wet Oxidation of Acetic Acid, Ind. Eng. Chem. Res. 37 (1998) 1203-1210.

[20] C.W. Hirt, B.D. Nichols, Volume of Fluid (VoF) method for the dynamics of free boundaries, J. Comput. Phys. 39 (1981) 201–225.

[21] W. Sabisch, Dreidimensionale numerische Simulation der Dynamik von Einzelblasen und Blasenschwärmen mit einer Volume-of-Fluid-Methode, Forschungszentrum Karlsruhe, FZKA 6478, June 2000.

[22] W. Sabisch, M. Wörner, G. Grötzbach, D.G. Cacuci, 3D volume-of-fluid simulation of a wobbling bubble in a gas-liquid system of low Morton number, Proc. Fourth Int. Conf. Multiphase Flow, May 27 – June 1, 2001, New Orleans, Louisiana, USA.

[23] M. Wörner, W. Sabisch, G. Grötzbach, D.G. Cacuci, Volume-averaged conservation equations for volume-of-fluid interface tracking, Proc. Fourth Int. Conf. Multiphase Flow, May 27 – June 1, 2001, New Orleans, Louisiana, USA.

[24] B. Ghidersa, Finite-Volume-based Volume-of-Fluid Method for the Simulation of Two-phase Flows in Small Rectangular Channels, Forschungszentrum Karlsruhe, FZKA 6889, 2003.

[25] S. Popinet, S. Zaleski, A front tracking algorithm for accurate representation of surface tension, Int. J. Num. Meth. Fluids 30 (1999) 775–793.

[26] M. Wörner, The influence of the gas-liquid density ratio on shape and rise velocity of an ellipsoidal bubble: a numerical study by 3D volume-of-fluid computations, Proc. First Int. Berlin Workshop on Transport Phenomena with Moving Boundaries, October, 11–12, 2001, Berlin, Germany, F.-P. Schindler (Ed.), Forschritt-Berichte VDI Reihe 3 Verfahrenstechnik Nr. 738, pp. 67-84, VDI Verlag GmbH, Düsseldorf 2002.

[27] M. Wörner, Invariance of the velocity field induced by a bubble rising steadily through liquid under variation of the gas-liquid density ratio, in: T. Schulenberg, M. Ozawa, G. Grötzbach, (Eds.) Proc. German-Japanese Workshop on Multiphase Flow, Karlsruhe, Germany, August 25–27, 2002, Forschungszentrum Karlsruhe, FZKA 6759, March 2003, pp. G10–G21.
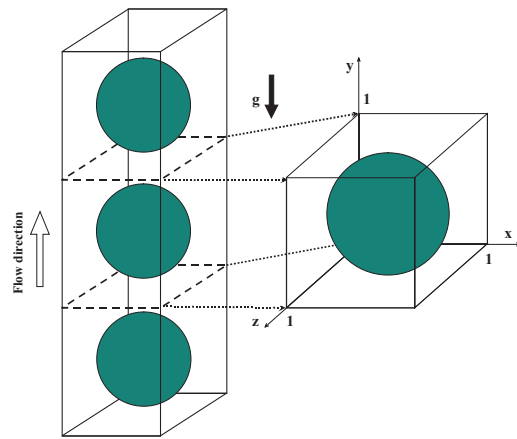
Fig. 1. Sketch of geometrical configuration and flow unit cell.

(a)   (b)

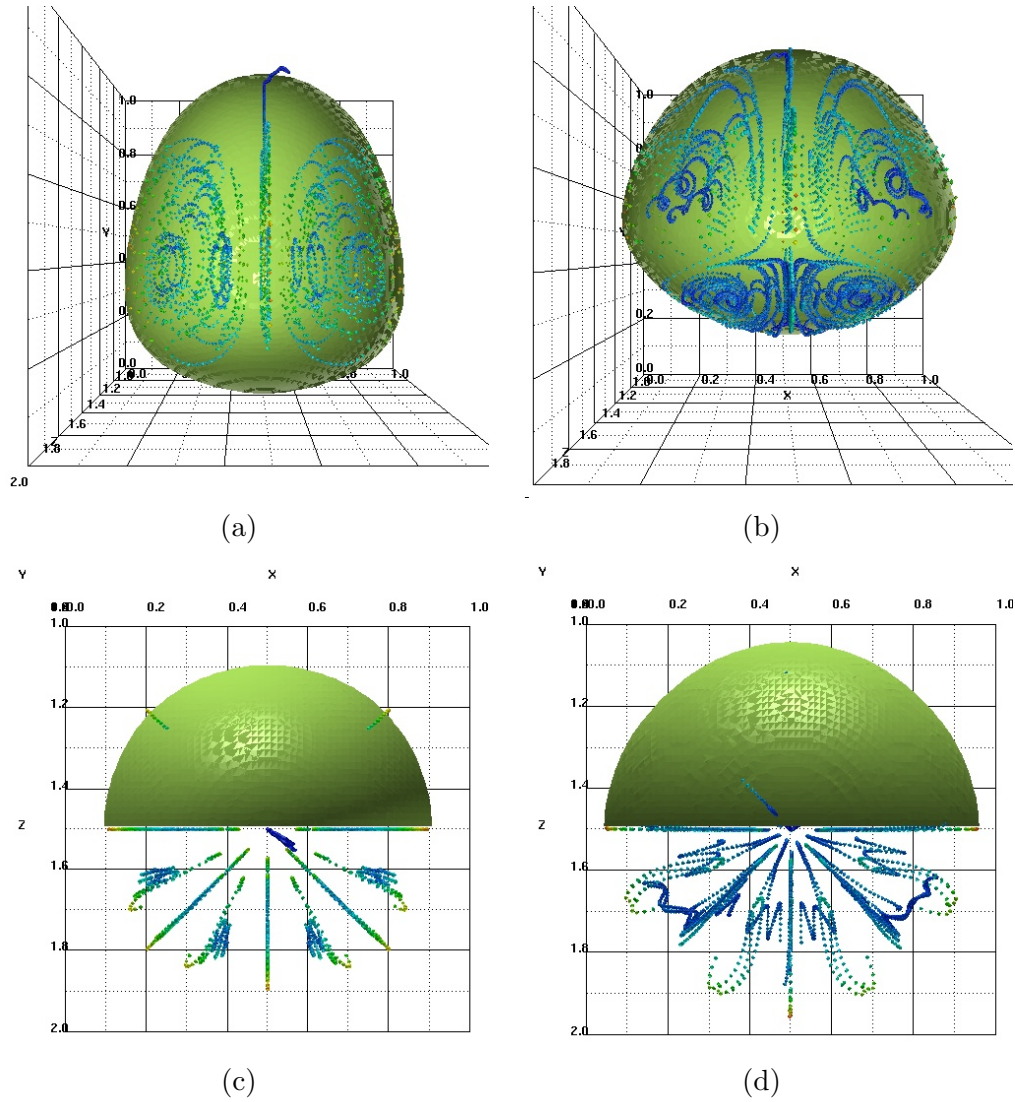(c)   (d)

Fig. 2. Visualization of half of the steady bubble shape and flow structure inside the bubble. View from side (Fig. a and b) and top (Fig. c and d) for case BT1 (Fig. a and c) and BT2 (Fig. b and d). The color of the particles is an indicator for the magnitude of the local velocity in the frame of reference moving with the bubble (blue = slow, red = fast).
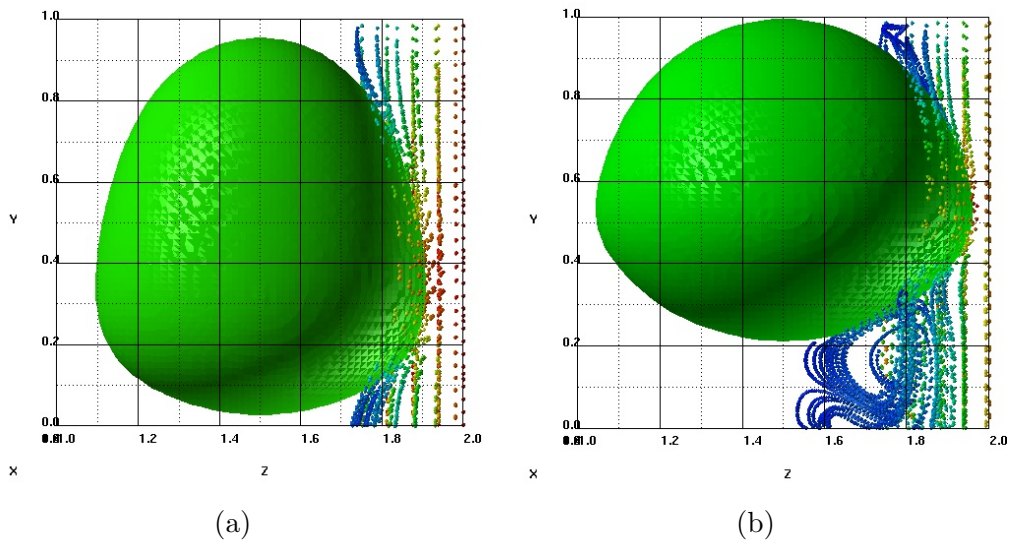
Fig. 3. Visualization of bubble shape and flow structure in the liquid (view from the side) for case BT1 (a) and BT2 (b). The color of the particles is an indicator for the magnitude of the local velocity in the frame of reference moving with the bubble (blue = slow, red = fast).
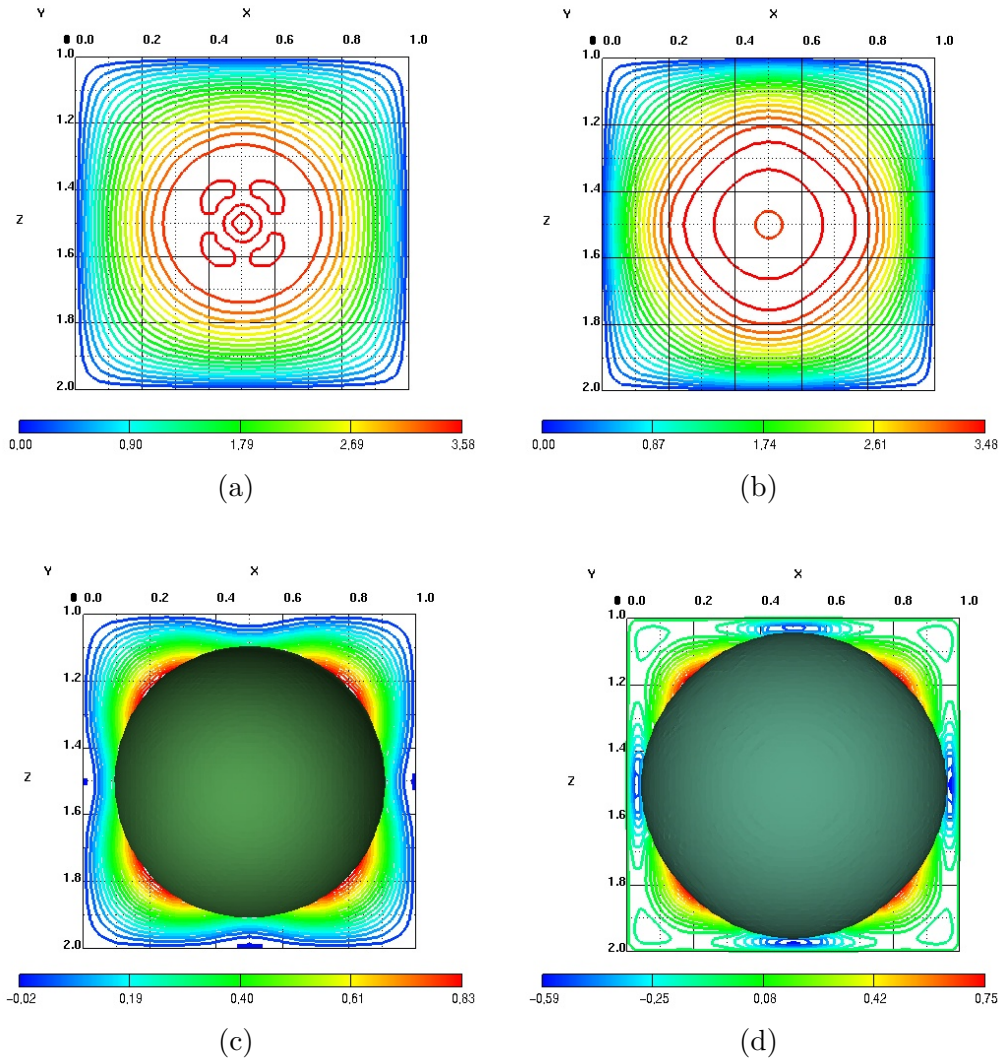
Fig. 4. Cross-sectional distribution of the non-dimensional axial velocity in a fixed frame of reference in the middle of the liquid slug (Fig. a and b) and in the stream-wise location with the thinnest film thickness (Fig. c and d) for case BT1 (Fig. a and c) and case BT2 (Fig. b and d).

Table 1
Fluid properties for case BT1 and BT2

Case	ρ_l^*	ρ_g^*	μ_l^*	μ_g^*	σ^*
BT1	957	11.7	0.048	0.000184	0.02218
BT2	913	11.7	0.0046	0.000184	0.02218

Table 2

Reference scales and code input parameters

Case	L^*_{ref}	U^*_{ref}	Re_{ref}	Eo_{ref}	We_{ref}	Eu_{ref}
BT1	0.002	0.0264	1.05	1.67	0.060	27.0
BT2	0.002	0.0626	24.85	1.59	0.323	0.20

Table 3

Numerical parameters and global non-dimensional simulation results

Case	grid	Δt	N_t	Ca_B	Re_B	D_B	J_l	J_g	V	W
BT1	48^3	2.5×10^{-5}	24,000	0.206	3.086	0.814	0.807	1.189	1.796	0.443
BT1	64^3	10^{-5}	60,000	0.205	3.075	0.812	0.806	1.189	1.80	0.445
BT2	64^3	10^{-4}	14,000	0.043	75.88	0.919	1.04	1.10	1.55	0.355